



Federated attention contrastive learning models for prostate cancer diagnosis and Gleason grading

2024

Fei Kong^{a,1}, Xiyue Wang^{b,1}, Jinxi Xiang^{c,1}, Sen Yang^c, Xinran Wang^d, Meng Yue^d, Jun Zhang^c, Junhan Zhao^{e,f,g}, Xiao Han^c,
Yuhan Dong^a, Biyue Zhu^h, Fang Wangⁱ, Yueping Liu^d^aShenzhen International Graduate School, Tsinghua University, Shenzhen, 518055, China^bCollege of Biomedical Engineering, Sichuan University, Chengdu, 610065, China^cAI Lab, Tencent, Shenzhen, 518057, China^dDepartment of Pathology, The Fourth Hospital of Hebei Medical University, Shijiazhuang, 050035, China^eMassachusetts General Hospital, Boston, MA, 02114, United States^fHarvard T.H. Chan School of Public Health, Boston, MA, 02115, United States^gDepartment of Biomedical Informatics, Harvard Medical School, Boston, MA, 02115, United States^hDepartment of Pharmacy, Children's Hospital of Chongqing Medical University, Chongqing, 400014, China.ⁱDepartment of Pathology, The Affiliated Yantai Yuhuangding Hospital of Qingdao University, Yantai, 264000, China

arXiv:2302.06089v4 [cs.CV] 29 Feb 2024 ARTICLE INFO

Article history:

Keywords:

Histopathology
Cancer detection
Federated learning
Contrastive learning
Attention mechanism

ABSTRACT

Artificial intelligence (AI) shows great promise in revolutionizing medical imaging, improving diagnosis, and refining treatment methods. However, the training of AI models relies on extensive multi-center datasets, presenting a potential challenge due to concerns about data privacy protection. Federated learning offers a solution by enabling a collaborative model across multiple centers without sharing raw data. In this study, we present a Federated Attention Contrastive Learning (FACL) framework designed to address challenges associated with large-scale pathological images and data heterogeneity. FACL improves model generalization by maximizing attention consistency between the local client and the server model. To enhance privacy and validate robustness, we incorporate differential privacy by introducing noise during parameter transfer. We assess the effectiveness of FACL in cancer diagnosis and Gleason grading tasks using 19,461 whole slide images of prostate cancer sourced from multiple centers. In the diagnosis task, FACL achieves an area under the curve (AUC) of 0.9718, outperforming seven centers whose average AUC is 0.9499 when categories are relatively balanced. In the Gleason grading task, FACL attained a Kappa score of 0.8463, surpassing the average Kappa score of 0.7379 from six centers. In conclusion, FACL offers a robust, accurate, and cost-effective AI training model for prostate cancer pathology while maintaining effective data safeguards.

© 2024 Elsevier B. V. All rights reserved.

1. Introduction

Prostate cancer ranks as the second most prevalent cancer and the fifth leading cause of cancer-related deaths among men

[1]. The gold standard for solid tumor diagnostics involves examining hematoxylin and eosin (H&E) stained whole slide images (WSIs) [2–4]. Accurate diagnosis and Gleason grading of prostate cancer WSIs are essential for effective clinical management and treatment [5, 6]. Specifically, Gleason grading is the most reliable method to assess prostate cancer aggressiveness

¹These authors contributed equally to this paper.

[7–9]. However, interobserver and intraobserver variability in Gleason scores can lead to under or over-treatment of patients in real-world scenarios [5, 10]. Furthermore, manual diagnostic labeling of pathological images is time-consuming and costly [11–14].

Recent advancements in artificial intelligence (AI) have propelled its expanded utilization in pathological image diagnosis. Pioneering research studies have showcased the capability of AI to provide precise, cost-effective, and scalable solutions by automating the analysis of patient data [5, 15–17]. Numerous previous studies [11, 16, 18–21] have unequivocally validated AI models' effectiveness in diagnosing prostate cancer and performing Gleason grading tasks. However, it is important to note that these AI models necessitate a substantial amount of data for training to attain optimal performance [22–24]. As a result, a typical strategy involves the collection of data from multiple centers, including medical centers and hospitals, and subsequently training the AI models through a centralized learning process. Nevertheless, it is crucial to acknowledge that the transfer of extensive volumes of sensitive patient data among clinics, hospitals, and other medical institutions can potentially compromise patient privacy, and may run counter to data protection regulations. Moreover, there are notable technical challenges to overcome, such as ensuring efficient data transfer and addressing storage requirements, which present considerable hurdles in this endeavor [24, 25].

Federated learning (FL) represents an innovative paradigm in which models are trained by sharing model parameter updates from decentralized data sources [25–29]. Retaining data locally can effectively address issues related to excessive data transmission and data ownership [30]. By directly sharing model parameters rather than the private data of multiple centers, FL offers a promising solution for applications involving sensitive data. In general, FL training methods can be categorized into two types: (1) primary server and (2) peer-to-peer [31]. The key distinction lies in whether a primary server is employed to collect each client's model parameters. FL has demonstrated significant potential for sensitive data analytics across multiple healthcare domains [28]. Examples include electronic health records (EHR) [32–36], healthcare IoT (Internet of Things) [37, 38], drug discovery [39–41], and medical image analysis (e.g., X-ray, Ultrasound, CT, MRI, PET, WSIs) [42–51]. Despite the advantages of FL in the context of gigapixel WSIs [50, 52–54], significant challenges remain, particularly in ensuring robustness in the face of considerable heterogeneity among WSIs with a wide range of morphological variations.

Data heterogeneity across different centers, characterized by each local model possessing non-identically and independently distributed (Non-IID) data, presents a significant challenge in the field of FL [55]. The divergence between the training and test data distributions can substantially impact model robustness negatively [56]. Several studies have made notable progress in addressing the heterogeneity problem through the following approaches: (1) Variance reduction: Recent advancements in this area focus on balancing the data distribution obtained by centers from other centers [57], to reduce variance. This is achieved by considering various aspects such as param-

eters, update directions, or feature representations among local models [58]. (2) Global model update: To expedite model convergence and enhance robustness, adaptive optimization [59–61] or personalized optimization [62] techniques are employed during the model parameter aggregation process. However, it should be noted that these improvements do not specifically address the heterogeneity issue of histopathological images in FL. By employing these approaches, researchers have made significant strides in mitigating data heterogeneity challenges in FL. Nevertheless, additional research is required to address the unique characteristics and complexities associated with histopathological images in this context.

The accurate diagnosis of pathological images requires a detailed analysis of the distinctive features present within cancerous regions. In this study, we have integrated an attention mechanism into the foundational classification model to facilitate this meticulous examination. Moreover, to effectively mitigate the inherent heterogeneity in federated learning settings, we have introduced contrastive learning techniques into the attention distribution process of the model. Consequently, we propose a novel framework termed Federated Attention Contrastive Learning (FACL), specifically devised to bolster attention consistency between the local client models and the central server model. This augmentation is strategically aimed at enhancing the generalization capacity of the model, particularly towards unseen data instances. Moreover, while FL retains data locally, there is an inherent risk of private information leakage during the parameter transfer to the server [63, 64]. To address this concern, we incorporate the use of differential privacy [65] as a protective measure [66]. It is worth noting that most existing advancements in this field have been proposed and validated using a limited number of small-scale image datasets, such as MNIST, CIFAR-10, CIFAR-100, EMNISTL, and Tiny ImageNet [58, 60, 67]. To validate the effectiveness of our proposed model, we have curated a large-scale clinical dataset consisting of 19,461 WSIs obtained from multiple centers. Rigorous testing conducted on this dataset, specifically focusing on prostate cancer diagnosis and Gleason grading, demonstrates clinical-grade performance.

Our research makes significant contributions in the following areas:

(1) We proposed a novel FL framework named FACL, which ensures privacy preservation and minimizes unnecessary data transmission, aiming at achieving better diagnosis and Gleason grading of prostate cancer based on large-scale and multi-center pathology images.

(2) We introduced a contrastive attention algorithm to address heterogeneity among FL centers. This algorithm improves the model's generalization ability by maximizing attention consistency between local client and server models.

(3) To comprehensively evaluate our approach, we curated a large-scale clinical prostate cancer dataset comprising 19,461 WSIs from multiple medical centers. These diverse data distributions ensure that our evaluation captures the complexities inherent in real-world prostate cancer cases.

2. Related works

This section presents a comprehensive overview of federated and contrastive learning, with a specific emphasis on their applications in medical image analysis.

2.1. Federated learning

Following Google’s introduction of the FL framework FedAvg [59], it has undergone extensive development, particularly addressing challenging aspects such as non-independent and identically distributed and unbalanced properties.

To address the Non-IID problem, FedDif [57] introduced a diffusion mechanism where local models diffuse in the network, enabling them to learn data distributions beyond their initial experience before global aggregation. Following sufficient diffusion iterations, each local model accumulated personalized data distributions, resembling the effects seen with training identically and independently distributed data. ComFed [58] employed variance reduction techniques on the client side to streamline server aggregation, coupled with global adaptive update techniques for accelerated learning. FedRS [60] proposed the use of “Restricted Softmax” to control the update of missing class weights during the local process. FedDC [61] introduced a lightweight modification in the local training phase, employing an auxiliary local drift variable for tracking the gap between local and global model parameters. FedProx [68], as an improvement upon FedAvg, incorporated a proximal term into the local objective function. This addition significantly enhanced the stability of the method, showcasing its effectiveness. FedFAME [69] introduces a comprehensive framework centered on model contrastive learning, with a primary focus on tackling challenges related to local client data enhancement and Non-IID issues, particularly in domains like text and graphs. While these methods have significantly contributed to Non-IID problem-solving, it’s crucial to acknowledge their primary validation on conventional natural images. Consequently, these approaches might not seamlessly apply to the distinctive characteristics of large-scale pathological images prevalent in medical imaging datasets.

FL has garnered widespread recognition for its effectiveness and efficiency in healthcare applications. Dou *et al.* [45] exemplified the feasibility of FL in detecting COVID-19-related CT abnormalities through a multinational study, achieving external validation and demonstrating robust generalization on internal and external datasets. In another study, Guo *et al.* [47] introduced a cross-site MR image reconstruction model that aligns learned intermediate latent features between different source centers with the latent feature distribution at the target centers. This innovative approach contributes to enhancing the model’s performance and adaptability across diverse datasets. Pati *et al.* [25] applied FL to rare disease diagnosis, leveraging data from 71 centers across six continents. The outcome was an automated tumor boundary detector for rare glioblastoma, showcasing the efficacy and practicality of FL in a multicenter setting. Liu *et al.* [70] took a novel approach by combining FL and contrastive learning in experiments with small-sized medical images, introducing FedCL to address data heterogeneity challenges. It is crucial to note that FedCL’s multicenter approach

involves dividing a dataset into multiple subsets, essentially creating a pseudo multicenter. However, this algorithm faces limitations in performing feature extraction in every round on large-sized pathological images. These studies collectively underscore the potential of FL in revolutionizing healthcare, emphasizing its adaptability to diverse scenarios while acknowledging certain constraints in specific applications.

Table 1. FL implementation scenarios and associated datasets.

Reference	Application	Data (Number)
FedAvg [59]	Natural images	MNIST
		CIFAR-10
		Shakespeare
FedDif [57]	Natural images	MNIST
		FMNIST
		CIFAR-10
ComFed [58]	Natural images	CIFAR-10
FedRS [60]	Natural images	CIFAR-10
FedDC [61]	Natural images	CIFAR-10
FedProx [68]	Natural images	MNIST
		Sent140
		FEMNIST
		Shakespeare
FedFAME [69]	Natural images	CIFAR-10
		20NewsGroups
		Fashion-MNIST
		5AbstractsGroup
FedCL [70]	Medical images (X-ray)	5908 images
		Medical images (CT)
		10594 images
		Medical images (MR)
[45]	Medical images	3443 images
		(ET, TC, WT)
		6314 images
		Epi700 (661)
[24]	Pathological images	TCGA (632)
		DACHS (2448)
		QuASAR (2190)
		YCR BCIP (889)
		RCC (1184)
[31]	Pathological images	BRCA (2126)
		CCRCC (511)
		Kidney (424)
Prop-FFL[71]	Pathological images	Lung (1217)

Several studies have showcased the potential of FL in analyzing histopathological images. Saldanha *et al.* [24] employed the FL model to predict BRAF mutation status and microsatellite instability from H&E stained colorectal cancer pathology sections. Ming *et al.* [31] and Seyedeh *et al.* [72] both utilized FL and differential privacy to underscore its efficacy in safeguarding medical privacy data on the public dataset TCGA. Addressing the issue of fairness among participants, Hosseini *et al.* [71] introduced proportional fair federated learning (Prop-FFL) and substantiated its effectiveness on two pathological datasets. As shown in **Table 1**, FL finds predominant application in the realm of natural images. However, in the field of medical imaging, its usage is more common for non-pathological images.

Notably, when it comes to pathological images, public datasets are predominantly utilized. However, a prevalent limitation in FL research applied to histopathological images lies in the lack of data diversity. Many studies rely heavily on public datasets, thereby lacking comprehensive verification of actual clinical data.

2.2. Contrastive learning

Contrastive learning (CL) stands out as a potent paradigm for visual representation learning, captivating considerable research attention in recent years. Seminal frameworks like SimCLR [73] and MoCo [74] have paved the way for this method, sparking a wave of subsequent developments. At its essence, contrastive learning revolves around discrimination minimizing the distance between augmented view representations of the same image (termed positive pairs) while maximizing the distance between augmented views of different images (referred to as negative pairs) [67, 75]. This fundamental principle underlies the remarkable progress in contrastive learning.

In the healthcare domain, prior research has showcased performance enhancements with the application of contrastive learning in specific domains such as electronic health records (EHR) [76, 77], human activity recognition (HAR) [78], electrocardiography (ECG) [79] and medical image analysis [13, 80–83].

In histopathology image analysis, several studies have explored the application of contrastive learning to enhance performance. Wang *et al.* [13] devised a CL-based backbone model that integrates multiple sub-memories and incorporates population-level discrimination to diminish potential false negatives. They trained this model under the conventional contrastive learning assumption. Yan *et al.* [84] utilized a deep clustering algorithm to maximize similarity between instance and cluster projection representations through contrastive learning. Simultaneously, they learned semantic features and generated initial clusters from unlabeled WSI patches. Zhu *et al.* [85] introduced a novel framework, multi-instance reinforced contrastive learning (MuRCL), to deeply mine intrinsic semantic relations among different patches, thereby advancing WSIs classification. Fashi *et al.* [86] proposed a fully supervised contrastive learning setting to enhance representation robustness for WSIs classification and perform pretext searches and downstream tasks. However, these contrastive learning methods primarily focus on feature representation and have not yet been tested on large-scale, diverse histopathology image datasets. Therefore, we extend this concept beyond visual representation to attention contrastive model training.

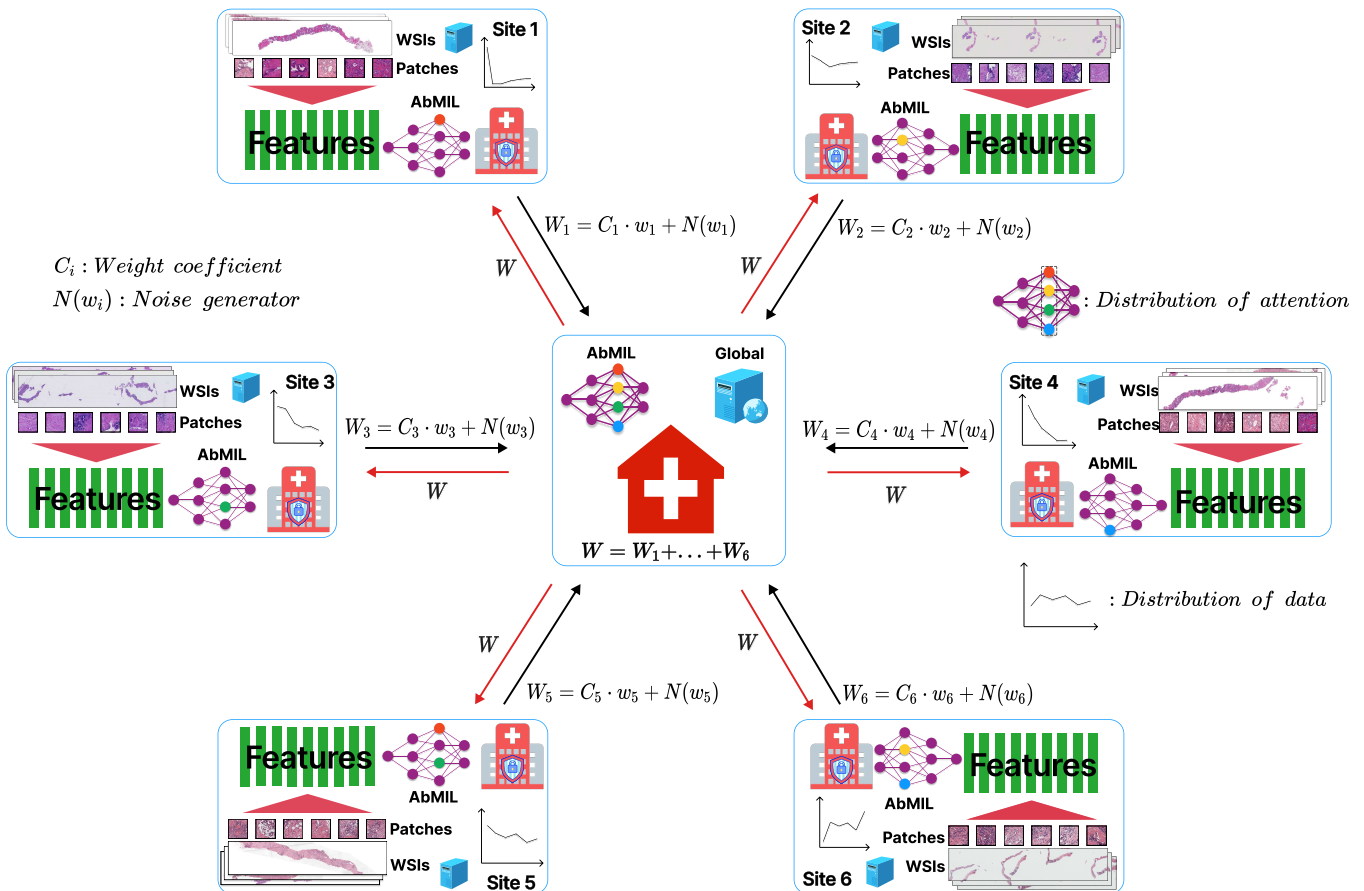


Fig. 1. The framework of feature extraction and model training process for FACL model on pathological images.

3. Methods

In this section, we provide an overview of the proposed FACL framework, as illustrated in **Fig. 1**. FL retains data locally on individual centers, allowing for patch-level segmentation and feature extraction of tissue regions directly on pathological images at the client level. In each client site, WSIs are cropped into patch images with a size of 224×224 pixels. Then, the Swin Transformer, augmented with convolutional operations, is employed to extract discriminative features. These features are then locally preserved as input for subsequent model training within the federated learning framework. Each client trains the model by transmitting model parameters to the central server. Subsequently, the server performs a weighted averaging upon collecting all client model parameters and then distributes the updated parameters to all centers for the next round of training. In addition to these procedures, we enhance dataset protection by incorporating differential privacy. This involves introducing random noise during the aggregation of model parameters at the server. Finally, to address the problem of unbalanced data distribution among centers, we also use the attention comparison to improve the consistency between the server and client models, which results in an improved final training model.

Initially, each client employs the CTransPath feature extractor [87] to acquire and store features from their local datasets. Subsequently, within the FACL framework, we integrate AttMIL [88], a weakly supervised model with an attention mechanism, for diagnosing and grading gigapixel WSIs with prostate cancer. This approach not only ensures patient privacy but also boosts the model's performance trained on individual client data. To tackle the Non-IID challenge, we introduce attention contrastive learning. Despite imbalanced data distribution among local centers, FACL can rectify these deviations, enabling the model to achieve optimal results.

3.1. Data preprocessing

High-resolution histopathology images often demand time-consuming analysis and are susceptible to interference from complex backgrounds [89]. An integral step in data processing involves cropping WSIs into smaller sizes suitable for model input. Removing the background region is crucial since it lacks informative content. We cropped patches (224×224 pixels) without overlap in regions with significant tissue presence, utilizing the Otsu thresholding method [90]. Subsequently, the features of each patch were extracted using the CTransPath feature extractor [87], and these features were aggregated for consolidated storage across the entire image. It is noteworthy that, unlike the ImageNet pre-trained model, the CTransPath extractor is pre-trained on multiple histopathology datasets.

3.2. Weakly-supervised learning on WSIs

At each local center, we employ a weakly supervised model, AttMIL, detailed in [88]. AttMIL integrates an attention mechanism, this model forms the basis for FL across local centers. **Fig. 2** depicts the attention mechanism pipeline, comprising three modules: f_{pro} for projection, f_{att} for attention, and f_{pre}

for prediction. We utilize the gating mechanism in conjunction with the $\tanh(\cdot)$ non-linearity. This mechanism enables the model to dynamically modulate the importance of different parts of the input sequence when making predictions. In this context, we utilize the feature vector extracted from CTransPath as the model's input. The attention mechanism facilitates the computation of attention scores for each instance, aiding in the identification of similarities or dissimilarities between instances. This approach, particularly relevant in computational pathology, provides interpretability and reasoning for regions of interest. This is particularly beneficial for medical professionals in the diagnosis of WSIs.

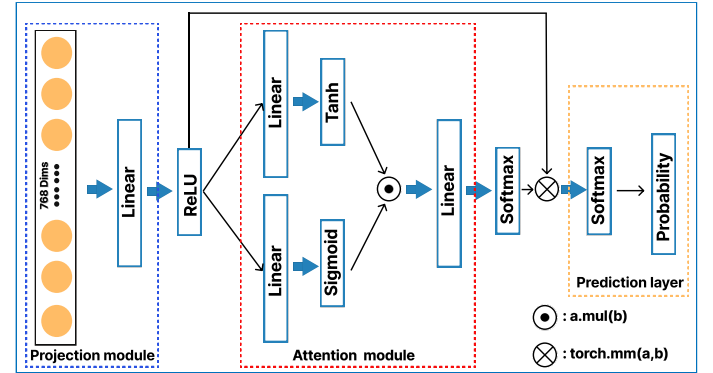


Fig. 2. The specific implementation details of the attention mechanism in FACL.

We provide detailed layer-by-layer explanations beginning with the projection module. This module, comprising contiguous, trainable, fully-connected layers, transforms fixed feature embeddings from a pre-trained encoder into a more compact feature space tailored to histopathology images related to the chosen disease model. The initial fully-connected layer $W_1 \in \mathbb{R}^{512 \times 768}$ compresses the 768-dimensional patch-level features z_k into a 512-dimensional vector $h_k = W_1 z_k^\top$. The resulting set of N patch-level h_k in a whole slide image is represented by $H \in \mathbb{R}^{N \times 512}$.

If we consider the first two attention matrices, U_a and V_a , both of dimensions $\mathbb{R}^{256 \times 512}$, as the shared attention backbone for all classes, the attention network can be divided into n parallel attention branches, denoted as $W_{a,1}, \dots, W_{a,n}$, each with dimensions $\mathbb{R}^{1 \times 256}$. Simultaneously, create n parallel independent classifiers, $W_{c,1}, \dots, W_{c,n}$, to assess each class-specific slide-level representation. The attention score for the k th patch of the m th class denoted as $a_{k,m}$ and computed by equation (1), contributes to the aggregation of the slide-level feature representation. The resulting slide-level feature representation for the m th class is denoted as $h_{slide,m} \in \mathbb{R}^{1 \times 512}$ and is computed by equation (2).

$$a_{k,m} = \frac{\exp \left\{ W_{a,m} (\tanh(V_a h_k^\top) \odot \text{sigm}(U_a h_k^\top)) \right\}}{\sum_{j=1}^N \exp \left\{ W_{a,m} (\tanh(V_a h_j^\top) \odot \text{sigm}(U_a h_j^\top)) \right\}} \quad (1)$$

$$h_{slide,m} = \sum_{k=1}^N a_{k,m} h_k \quad (2)$$

The slide-level score $s_{slide,m}$ is derived from the classification layer $W_{c,m} \in \mathbb{R}^{1 \times 512}$ through the formula $s_{slide,m} = W_{c,m} h_{slide,m}^\top$.

During inference, the predicted probability distribution for each class is obtained by applying the softmax function to the slide-level prediction scores.

3.3. Federated learning on WSIs

In this section, we elaborate on the details of the proposed federated attention contrastive learning method, as well as the differential privacy techniques used to provide additional protection to the model.

3.3.1. Federated attention contrastive learning

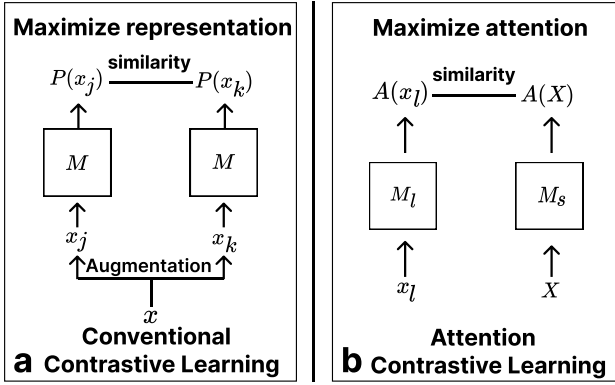


Fig. 3. Illustration of the difference between conventional contrastive learning and attention contrastive learning. $P(x)$ in (a) represents the representation of x . $A(x)$ in (b) represents the attention obtained by x through model M (M_l and M_s correspond to the client model and server model, respectively).

Inspired by contrastive learning, we considered applying it at the attention level. **Fig. 3** illustrates the fundamental difference between conventional contrastive learning and attention contrastive learning methods. In conventional contrastive learning, the model is trained to maximize the proximity of similar samples while maintaining a separation from dissimilar ones. A key feature of this learning method is that it does not require explicit label usage in the training process. In our attention contrastive learning, we integrate the characteristics of client and server models in the FL learning, aiming to maximize the consistency between the attention scores of the local client model and that of the server model. This ensures that a center model indirectly acquires the attentional insights of other centers' models through the intermediary server. Based on attention contrastive learning, we propose FACL by combining the FedAvg [59] and weakly supervised learning. It introduces lightweight and efficient modifications in client-side training. Each client trains a relatively personalized model during local training due to data heterogeneity. The server's global model, in turn, acquires a significantly improved representation compared to the local model. The aim of FACL is to bolster the learning and generalization capabilities of the client-side model by augmenting the consistency between the *attention* learned by the client-side model and that acquired by the server-side model.

The loss of the local model consists of two components. The first part is the standard loss, such as cross-entropy loss in supervised learning, denoted as \mathcal{L}_{CE} in this paper. The second part is the contrastive loss, denoted as \mathcal{L}_{FACL} , which measures the disparity between the attention scores of client-side models and the server-side model. Given the predicted probability value of the classification model as "logits," the label as "y," and the attention scores of the local model and the server model as A_{local} and A_s , respectively, the total loss can be expressed as follows:

$$\mathcal{L} = \mathcal{L}_{CE}(logits, y) + \mu \mathcal{L}_{FACL}(A_{local}, A_s), \quad (3)$$

$$\mathcal{L}_{FACL} = KL[P(X) \parallel Q(X)] = \sum_{x \in X} [P(x) \log \frac{P(x)}{Q(x)}], \quad (4)$$

Here, μ represents the hyperparameter controlling the weight

Algorithm 1: Pseudocode of FACL algorithm

```

Input: WSIs Data and weak annotation ( $X, Y$ );
Output: Global model  $f_{server}(f_s)$ ;
1 Initialize all model parameters  $\{W_g^0, W_1^0, \dots, W_M^0\}$  ;
  // Training  $K$  rounds
2 for  $k = 1$  to  $K$  do
  //  $M$  independent centers
 3   for  $i = 1$  to  $M$  do
    //  $N_i$  WSIs
    4     for  $j = 1$  to  $N_i$  do
      // Local model projection
      5        $H_{i,j} = f_{pro}(X'_{i,j})$  ;
      // Server model projection
      6        $H_s = f_{s,pro}(X'_{i,j})$  ;
      // Local model attention
      7        $A_{i,j} = f_{att}(H_{i,j})$  ;
      // Server model attention
      8        $A_s = f_{att}(H_s)$  ;
      // Feature representation of the WSI
      9        $h_{bag} = W\text{-Ave}(A_{i,j}, H_{i,j})$  ;
      // Output predicted value
      10       $s_{i,j} = f_{pre}(h_{bag_{i,j}})$  ;
      // Calculate attention similarity
      11       $\mathcal{L}_{FACL}(A_{i,j}, A_s) = KL[A_{i,j} \parallel A_s]$  ;
      // Calculate loss function
      12       $\mathcal{L} = \mathcal{L}_{CE}(s_{i,j}, Y_{i,j}) + \mu \mathcal{L}_{FACL}(A_{i,j}, A_s)$  ;
      // Optimize model parameters
      13       $W_i \leftarrow \text{Opt}_i(\mathcal{L}, W_i)$  ;
      // Update server parameters
      //  $\gamma_i$ :Weight coefficient
      //  $N_g(W)$ :Noise generator
      14       $W_s \leftarrow \sum_i \gamma_i(W_i) + N_g(W_i)$  ;
      // Update local model parameters
      15      for  $i = 1$  to  $M$  do
        //  $W_i \leftarrow W_s$  ;
      16
    17 return  $f_s$ 

```

of the attention contrastive loss. \mathcal{L}_{FACL} denotes the Kullback-Leibler divergence [91], quantifying the similarity between two probability distributions.

3.3.2. FACL with differential privacy

By embracing the principles of data differential privacy, we seamlessly integrated this approach into the FL server, specifically during the phase where the server receives parameter updates from individual client models. The crux of differential privacy involves introducing noise to the model weights before transmitting them to the centralized server. To execute this, we utilized a noise generator denoted as $N_g(\cdot)$, generating Gaussian random noise $\mathbf{Z} \sim (0, z^2\eta^2)$, with z denoting the noise level and η representing the standard deviation of the neural network weight.

The noise is carefully calibrated to prevent significant degradation of learned weights or overall model performance. Striking the right balance involves introducing sufficient noise to safeguard privacy while enabling the model to extract valuable information [51, 92]. In FL, noisy weight updates from multiple centers are consolidated on the server. The noise introduced by each center tends to offset when combined, resulting in a more precise global model. This occurs because the noise is typically drawn from a distribution with a mean of zero, leading to an averaging effect when aggregated from different centers. Although the introduction of noise in the weights may marginally influence learned weights, the FL is designed to minimize this impact.

Table 2. Data distribution used for cancer diagnosis. (x% denotes the proportion of positive slides)

Center	WSIs No.	Train No.	Val No.
Hebei-1	1201 (21%)	960	241
Hebei-2	844 (73%)	675	169
Nanchang	983 (90%)	786	197
DiagSet-B-1	2313 (45%)	1850	463
DiagSet-B-2	2313 (45%)	1850	463
PANDA-1	5453 (65%)	4362	1091
PANDA-2	5159 (81%)	4127	1032

By strategically managing added noise and aggregating updates from multiple centers, FACL effectively maintains commendable model performance while ensuring privacy. In our investigation, we aimed to strike a delicate balance between privacy preservation and model efficacy. We conducted experiments introducing noise at varying magnitudes, discovering that a noise factor of $z = 0.1$ provides optimal protection without compromising the overall performance of the model. The culmination of our efforts is encapsulated in the proposed FACL algorithm, integrating contrastive learning and differential privacy, detailed in **Algorithm 1**. In each iteration, the server disseminates the global model to all participating parties

for localized training. Subsequently, the updated local models from each party contribute to refining the global model through a weighted average. We denote the number of rounds of FL training as K . Please assume that the WSIs data and its weakly supervised labels are distributed over M independent centers: $(\mathbf{X}, \mathbf{Y}) = \{(\mathbf{X}_{1,j}, Y_{1,j}), \dots, (\mathbf{X}_{M,j}, Y_{M,j})\}$, where $\{(\mathbf{X}_{i,j}, Y_{i,j})\} = \{(\mathbf{X}_{i,1}, Y_{i,1}), \dots, (\mathbf{X}_{i,N_i}, Y_{i,N_i})\}$ denotes the N_i pair of WSIs data and the corresponding labels for the i th client center, $\mathbf{X}_{i,j}$ is a single WSI. After data preprocessing and feature extraction, the data are represented as $(\mathbf{X}', \mathbf{Y}) = \{(\mathbf{X}'_{1,j}, Y_{1,j}), \dots, (\mathbf{X}'_{M,j}, Y_{M,j})\}$. The server-side model is f_s and the local client's neural network model $f_{center} = \{f_1, \dots, f_M\}$. Each model f_i contains a projection module $f_{i,pro}$, an attention module $f_{i,att}$, and a prediction layer $f_{i,pre}$. W-Ave: Use the attention scores predicted by all patches as weights to average the feature embeddings of all patches. The parameters of the local model are denoted as $\mathbf{W}_1, \dots, \mathbf{W}_M$, and the parameters of the global model are \mathbf{W}_g . Opt_i is an optimizer that updates the model parameters.

4. Experiments and results

This section introduces the datasets used for prostate cancer diagnosis and Gleason grading tasks. We provide details on data distribution and the experimental setup. Additionally, we assess the effectiveness of FL in both diagnostic and Gleason grading tasks. We compare performance differences between FedAvg and single-center models, as well as between FACL and FedAvg. To enhance interpretability, we employ a heatmap to visualize cancerous regions identified by the model.

4.1. Datasets

In this study, we delved into the diagnosis of prostate cancer, adopting a two-level classification approach to differentiate between benign and malignant conditions. Furthermore, we examined the Gleason grading of prostate cancer, employing a six-level classification system based on the International Society of Urological Pathology (ISUP [15]) categories: 0, 1, 2, 3, 4, and 5. A series of preprocessing steps were implemented on the datasets to demonstrate the efficacy of the FL model. These steps aimed to enhance the heterogeneity of the datasets by splitting those with a substantial number of samples into multiple independent centers, thus expanding the number of client centers within the FL model. The distribution of datasets utilized in the cancer diagnosis task is presented in **Table 2**, the DiagSet-B and PANDA datasets have been split into two separate centers, namely DiagSet-B-1, DiagSet-B-2, PANDA-1, and PANDA-2, with the proportion of positive data ranging from 21% to 90%. Similarly, the dataset distribution for

Table 3. Data distribution used for cancer diagnosis. (The x% represents the proportion of each class in the total data volume)

Center	WSIs No.	ISUP-0	ISUP-1	ISUP-2	ISUP-3	ISUP-4	ISUP-5
Hebei-1	1201	952 (79.3%)	18 (1.5%)	17 (1.4%)	42 (3.5%)	72 (6.0%)	100 (8.3%)
Hebei-2	844	220 (26.1%)	169 (20.0%)	88 (10.4%)	108 (12.8%)	125 (14.8%)	134 (15.9%)
PANDA-1-1	2727	962 (35.3%)	906 (33.2%)	334 (12.2%)	159 (5.8%)	241 (8.8%)	125 (4.6%)
PANDA-1-2	2727	962 (35.3%)	907 (33.3%)	334 (12.2%)	158 (5.8%)	240 (8.8%)	126 (4.6%)
PANDA-2-1	2580	484 (18.8%)	426 (16.5%)	338 (13.1%)	462 (17.9%)	384 (14.9%)	486 (18.8%)
PANDA-2-2	2579	483 (18.7%)	426 (16.5%)	337 (13.1%)	462 (17.9%)	384 (14.9%)	487 (18.9%)

Gleason grading is illustrated in **Table 3**, the PANDA datasets have been split into four separate centers, namely PANDA-1-1, PANDA-1-2, PANDA-2-1, and PANDA-2-2, where the categories of ISUP 0-5 exhibit a notable imbalance. According to the definition of federated learning classification, our work used horizontal federated learning [93].

For the prostate cancer diagnosis task, we curated datasets from three hospitals (Hebei-1, Hebei-2, Nanchang) and two public sources (DiagSet-B, PANDA) for training purposes. To evaluate the effectiveness of our approach, we used a private hospital dataset (QHD) and a public dataset (DiagSet-A) for testing. Hebei-1 and Hebei-2 are two hospital datasets from Hebei Province, China. Nanchang is a hospital dataset from Nanchang, China. The QHD dataset, sourced from a hospital in Qinhuangdao, China, comprises a total of 765 pathological images, with 433 of them being positive. DiagSet-A, a subset of the DiagSet data, comprises 430 pathological images, with 227 of them being positive.

To assess the accuracy of prostate cancer Gleason grading, we employed two private datasets (Hebei-1, Hebei-2) and one public dataset(PANDA) for training purposes. For the evaluation phase, we employed a private hospital dataset (Nanchang). This allowed us to gauge the performance and reliability of our approach.

4.2. Experimental setups and evaluation metrics

We utilized the loss functions and algorithmic models outlined in Section 3.3 for each task. As an illustration, we conducted a simulated FL experiment employing 8 Tesla V100 GPUs, with each card representing an independent center. In this experiment, we employed a learning rate of 0.0002, an Adam optimizer, and a batch size of 1. To ensure optimal results, we trained the model for 60 epochs. Additionally, we implemented an early stopping strategy, halting training when the server model failed to demonstrate improvement after 20 consecutive epochs while ensuring a minimum of 40 epochs were completed. To promote convergence toward optimal outcomes, we calculated validation metrics for each epoch and selected the model with the highest performance on the validation set for the final evaluation of the test set. Our experiments encompassed three distinct settings: (1) Local Learning: Each center independently trained its data. (2) Global Learning: Aggregating datasets from all centers, we trained a multicenter centralized model. (3) Federated Learning: Training on data from all centers without sharing datasets, focusing solely on exchanging model parameters. By employing these strategies, we aimed to refine our approach and ensure a comprehensive evaluation of our model across different learning scenarios.

Table 4. The proportion of positive data across four centers.

α	DiagSet-B-1	DiagSet-B-2	PANDA-1	PANDA-2
0.05	50/1000	50/1000	75/1500	1425/1500
0.1	100/1000	100/1000	150/1500	1350/1500
0.3	300/1000	300/1000	450/1500	1050/1500
0.5	500/1000	500/1000	750/1500	750/1500

The distribution of data splits for the diagnostic task is outlined in **Table 4**. To assess the impact of data imbalance on the model's performance, we partitioned the dataset from four centers (DiagSet-B-1, DiagSet-B-2, PANDA-1, PANDA-2), which contains a substantial number of samples, into positive proportions denoted as α (specifically, $\alpha = 0.05, 0.1, 0.3, 0.5$). It is worth noting that we focused on conducting this verifica-

Table 5. The performance of the diagnostic model on the validation set was reported as the mean of five-fold cross-validation results. ($\mu=0.1, z=0.1$)

α	Training settings	AUC	F1	ACC	Recall
0.05	Hebei-1	0.9487	0.8481	0.8325	0.7450
	Hebei-2	0.9422	0.8973	0.8698	0.8981
	Nanchang	0.9410	0.8685	0.8174	0.9303
	DiagSet-B-1	0.9222	0.7917	0.7830	0.6633
	DiagSet-B-2	0.9385	0.7679	0.7620	0.6264
	PANDA-1	0.9510	0.8999	0.8821	0.8426
	PANDA-2	0.9312	0.8439	0.7716	0.9622
	Avg. (7 centers)	0.9393	0.8453	0.8169	0.8097
	Centralized	0.9680	0.9291	0.9129	0.9022
	FedAvg	0.9620	0.9247	0.9083	0.8887
0.1	FedAvg(z)	0.9633	0.9248	0.9089	0.8855
	FACL (μ)	0.9626	0.9260	0.9096	0.8936
	FACL (μ, z)	0.9635	0.9256	0.9099	0.8859
	DiagSet-B-1	0.9402	0.8419	0.8273	0.7326
	DiagSet-B-2	0.9513	0.8177	0.8054	0.6965
	PANDA-1	0.9487	0.9012	0.8838	0.8387
	PANDA-2	0.9514	0.8830	0.8390	0.9555
	Avg. (7 centers)	0.9462	0.8654	0.8393	0.8281
	Centralized	0.9762	0.9392	0.9251	0.9152
	FedAvg	0.9691	0.9326	0.9179	0.8963
0.3	FedAvg(z)	0.9708	0.9304	0.9160	0.8876
	FACL (μ)	0.9701	0.9343	0.9201	0.8976
	FACL (μ, z)	0.9715	0.9345	0.9204	0.8970
	DiagSet-B-1	0.9595	0.8583	0.8422	0.7566
	DiagSet-B-2	0.9436	0.8415	0.8269	0.7324
	PANDA-1	0.9570	0.9176	0.8946	0.9257
	PANDA-2	0.9566	0.9143	0.8898	0.9257
	Avg. (7 centers)	0.9498	0.8780	0.8533	0.8448
	Centralized	0.9842	0.9511	0.9397	0.9265
	FedAvg	0.9725	0.9382	0.9245	0.9059
0.5	FedAvg(z)	0.9722	0.9341	0.9198	0.8977
	FACL (μ)	0.9731	0.9420	0.9291	0.9099
	FACL (μ, z)	0.9743	0.9447	0.9318	0.9202
	DiagSet-B-1	0.9522	0.8801	0.8634	0.7971
	DiagSet-B-2	0.9570	0.8934	0.8768	0.8202
	PANDA-1	0.9572	0.8977	0.8596	0.9440
	PANDA-2	0.9516	0.9144	0.8947	0.8873
	Avg. (7 centers)	0.9499	0.8856	0.8592	0.8603
	Centralized	0.9837	0.9540	0.9428	0.9371
	FedAvg	0.9671	0.9386	0.9242	0.9148

tion solely within the realm of binary classification, primarily due to significant variations in the quantity and category of datasets. As such, we did not undertake a similar distribution experiment within the context of multi-category classification. Consequently, the simulation experiment of FL involved seven centers. Each center's dataset was randomly divided into training and validation sets with an 80% and 20% ratio. Stratified sampling was employed to ensure a consistent class balance between each center's training and validation sets. Furthermore, to evaluate the model's robustness and generalization on previously unseen datasets, we utilized datasets from two independent centers for testing. In the case of the Gleason grading task, we implemented a FL model with six centers. We employed an independent dataset obtained from a private institution for testing purposes. On diagnostic and Gleason grading tasks, we evaluated the proposed FACL model using a variety of classification metrics, including AUC, F1 score, ACC, Recall, and Kappa score.

4.3. Results of diagnosis (Binary classification)

In the diagnostic task, we assessed models trained on datasets with varying degrees of heterogeneity, as indicated by the proportion factor $\alpha = \{0.05, 0.1, 0.3, 0.5\}$ in **Table 4**. Our experiments aimed to validate the performance of each local center model, FedAvg model, FACL model, and *Centralized* model across seven internal datasets and two external datasets (DiagSet-A and QHD).

4.3.1. Internal datasets

The experimental results for the diagnosis task on the validation set are presented in **Table 5**, showcasing metrics such as AUC, F1, ACC, and Recall. Due to the different proportions of categories in the diagnostic task, the local center model's overall performance is getting better with the increase of α . When α is 0.05, the average ACC of 7 centers (Hebei-1, Hebei-2, Nanchang, DiagSet-B-1, DiagSet-B-2, PANDA-1, PANDA-2)

model is only 0.8169, and the average AUC is only 0.9393. When α is 0.5, the average ACC of 7 centers (Hebei-1, Hebei-2, Nanchang, DiagSet-B-1, DiagSet-B-2, PANDA-1, PANDA-2) model reaches 0.8592, and the average AUC reaches 0.9499.

We observed superior performance in FL models compared to local center models. Specifically, the FACL model demonstrated a notable enhancement in AUC ranging from 0.02 to 0.04 when compared to individual centers. The deviation in results between the FACL model and the *Centralized* model is minimal, with less than a 0.01 difference in AUC. This outcome suggests that the FACL model has achieved an optimal value in line with federated learning theory, closely aligning with the performance of the *Centralized* model.

4.3.2. External datasets (DiagSet-A and QHD)

WSIs can vary widely in morphological appearance due to differences in institutional standards and protocols for tissue processing, slide preparation, and digitization of pathological images. Therefore, it is important to generalize the model application to actual clinical data. We validate the robustness of the model using two external datasets. We found that models trained using FL on multiple center data significantly improved the generalization performance of the models compared to models trained on single-center data.

The FedAvg and FACL model on the test set is presented in **Table 6**. The FACL model demonstrates superior AUC performance compared to the FedAvg model on both DiagSet-A and QHD datasets. On the DiagSet-A dataset, FACL (μ, z) achieves optimal results, demonstrating its effectiveness. Additionally, on the QHD dataset, FACL (μ) achieves optimal results without added noise. However, even when noise is introduced in FACL (μ, z), the results remain highly satisfactory. The comparison results between the single-center model and the *Centralized* model can be found in Tables S1 and S2 in the appendix.

Table 6. Comparison results between FedAvg and FACL on DiagSet-A and QHD sets. ($\mu=0.1, z=0.1$)

α	FL models	DiagSet-A			QHD				
		AUC	F1	ACC	Recall	AUC	F1	ACC	Recall
0.05	FedAvg	0.9635	0.9079	0.8969	0.9559	0.9795	0.9439	0.9346	0.9722
	FedAvg (z)	0.9632	0.9156	0.9063	0.9559	0.9804	0.9491	0.9411	0.9699
	FACL (μ)	0.9666	0.9188	0.9110	0.9471	0.9825	0.9461	0.9372	0.9722
	FACL (μ, z)	0.9674	0.9148	0.9063	0.9471	0.9824	0.9379	0.9267	0.9769
0.1	FedAvg	0.9648	0.9204	0.9133	0.9427	0.9775	0.9426	0.9333	0.9676
	FedAvg (z)	0.9651	0.9135	0.9063	0.9251	0.9782	0.9553	0.9490	0.9630
	FACL (μ)	0.9678	0.9091	0.9016	0.9251	0.9758	0.9486	0.9411	0.9607
	FACL (μ, z)	0.9687	0.9164	0.9086	0.9427	0.9766	0.9466	0.9385	0.9630
0.3	FedAvg	0.9651	0.8972	0.8852	0.9427	0.9788	0.9523	0.9451	0.9699
	FedAvg (z)	0.9664	0.9121	0.9016	0.9603	0.9789	0.9490	0.9411	0.9676
	FACL (μ)	0.9710	0.9048	0.8946	0.9427	0.9801	0.9500	0.9424	0.9653
	FACL (μ, z)	0.9741	0.9063	0.8969	0.9383	0.9792	0.9239	0.9098	0.9676
0.5	FedAvg	0.9647	0.8957	0.8805	0.9647	0.9765	0.9522	0.9451	0.9676
	FedAvg (z)	0.9661	0.9012	0.8875	0.9647	0.9783	0.9478	0.9398	0.9653
	FACL (μ)	0.9718	0.8934	0.8782	0.9603	0.9796	0.9457	0.9372	0.9653
	FACL (μ, z)	0.9725	0.8915	0.8735	0.9779	0.9762	0.9170	0.9006	0.9699

Table 7. The performance of the Gleason grading model on the validation set was reported as the mean of a five-fold cross-validation. ($\mu=0.1$, $z=0.1$)

Training settings	Kappa	AUC	F1	Recall
Hebei-1	0.6491	0.7679	0.3699	0.4589
Hebei-2	0.6977	0.7989	0.4787	0.5040
PANDA-1-1	0.8094	0.8866	0.6176	0.6367
PANDA-1-2	0.7531	0.8716	0.5476	0.5772
PANDA-2-1	0.7633	0.8748	0.6007	0.6218
PANDA-2-2	0.7552	0.8684	0.5794	0.6122
Avg. (6 centers)	0.7379	0.8447	0.5323	0.5684
Centralized	0.8779	0.9373	0.7490	0.7515
FedAvg	0.8494	0.9212	0.7158	0.7197
FedAvg (z)	0.8444	0.9136	0.6877	0.6951
FACL (μ)	0.8535	0.9214	0.7201	0.7251
FACL (μ, z)	0.8463	0.9126	0.6892	0.6969

4.4. Results of Gleason grading (Multiple classifications)

Given the scarcity of ISUP-annotated datasets, we assess the performance of local center models, the FedAvg model, the FACL model, and the Centralized model on five internal datasets and an external dataset (Nanchang).

4.4.1. Internal datasets

The validation set results for the Gleason scoring task are presented in **Table 7**. In comparison with models trained on single-center data, the FACL model exhibits significant improvements in Kappa score and AUC. The average Kappa across six centers (Hebei-1, Hebei-2, PANDA-1-1, PANDA-1-2, PANDA-2-1, PANDA-2-2) was 0.7379, whereas FACL achieved a Kappa of 0.8463. This highlights the effectiveness of federated learning in diagnosing prostate cancer across multiple categories. Notably, our proposed FACL model consistently outperforms the FedAvg model in Kappa score, regardless of the addition of noise (z). The Kappa scores for FACL (μ) surpass FedAvg, and FACL (μ, z) outperform FedAvg (z). This underscores the efficacy of our attention contrastive learning method.

4.4.2. External datasets (Nanchang)

Table 8. The Gleason grading model's performance on Nanchang was reported as the five-fold mean.

Training settings	Kappa	AUC	F1	Recall
Hebei-1	0.5494	0.7540	0.3107	0.3581
Hebei-2	0.6142	0.7862	0.3652	0.3977
PANDA-1-1	0.7052	0.8259	0.4525	0.4954
PANDA-1-2	0.6346	0.8423	0.3242	0.3794
PANDA-2-1	0.6649	0.8186	0.3648	0.4292
PANDA-2-2	0.6936	0.8307	0.3326	0.4374
Avg. (6 centers)	0.6437	0.8096	0.3583	0.4162
FedAvg	0.7247	0.8435	0.4552	0.4954
Centralized	0.7171	0.8365	0.4301	0.4638

The Kappa score exhibited a notable enhancement in the Gleason scoring task, as detailed in **Table 8**. Across the six

centers, the average Kappa score reached 0.6437, while FedAvg achieved a Kappa score of 0.7247. Notably, FedAvg's Kappa outperforms even the *Centralized* model, underscoring the robustness of models trained through federated learning. The comparative results of FedAvg and FACL models on the test set (Nanchang) are presented in **Table 9**. With the integration of an attention comparison mechanism, the FACL model demonstrates superior performance compared to FedAvg. FACL (μ) achieves a Kappa score of 0.7298, surpassing FedAvg's 0.7247, and FACL (μ, z) at 0.7342 outperforms FedAvg (z) at 0.7227. This emphasizes the effectiveness of the attention contrastive learning mechanism introduced in the FACL model.

Table 9. Comparison results between FedAvg and FACL on the Nanchang set. ($\mu=0.1$, $z=0.1$)

FL models	Kappa	AUC	F1	Recall
FedAvg	0.7247	0.8435	0.4552	0.4954
FedAvg(z)	0.7227	0.8513	0.4448	0.4944
FACL (μ)	0.7298	0.8451	0.4403	0.4883
FACL (μ, z)	0.7342	0.8521	0.4376	0.4842

4.5. Interpretability and whole slide attention visualization

To assess the effectiveness of our proposed model in capturing morphological features of prostate cancer, a random subset of WSIs was selected from the test set. Heatmaps, as shown in **Fig. 4**, were generated using a patch size of 224×224 and a 90% overlap. Each patch's attention score was normalized to the range $[0, 1]$, with high scores indicating regions crucial for diagnosis. To enhance clarity, RGB color maps were applied, with red representing high attention and blue indicating low attention. These heatmaps were then overlaid onto the original WSIs.

5. Conclusion

We proposed a novel FL model, referred to as FACL, designed for the diagnosis and Gleason grading of prostate cancer based on pathology images. We incorporated model attention comparison to enhance consistency between the server and client models, resulting in improved robustness and accuracy of the trained models. Additionally, to prevent malicious centers from inferring other centers' data during the model training process and to safeguard the privacy of both model builders and data providers, we introduced noise to the model using differential privacy. This approach strikes a balance between privacy protection and model performance. While FACL has made strides in addressing privacy concerns for large-sized medical data, our work still has some limitations. First, we validated the model's effectiveness only on prostate pathological images. The model's performance can be further verified by testing on WSI datasets containing more diverse cancer types. Second, the number of private medical dataset centers we used remains relatively small. In the future, we aim to extend the application of FL to a wider range of medical diagnostic tasks in various medical scenarios. For instance, we envision its utilization

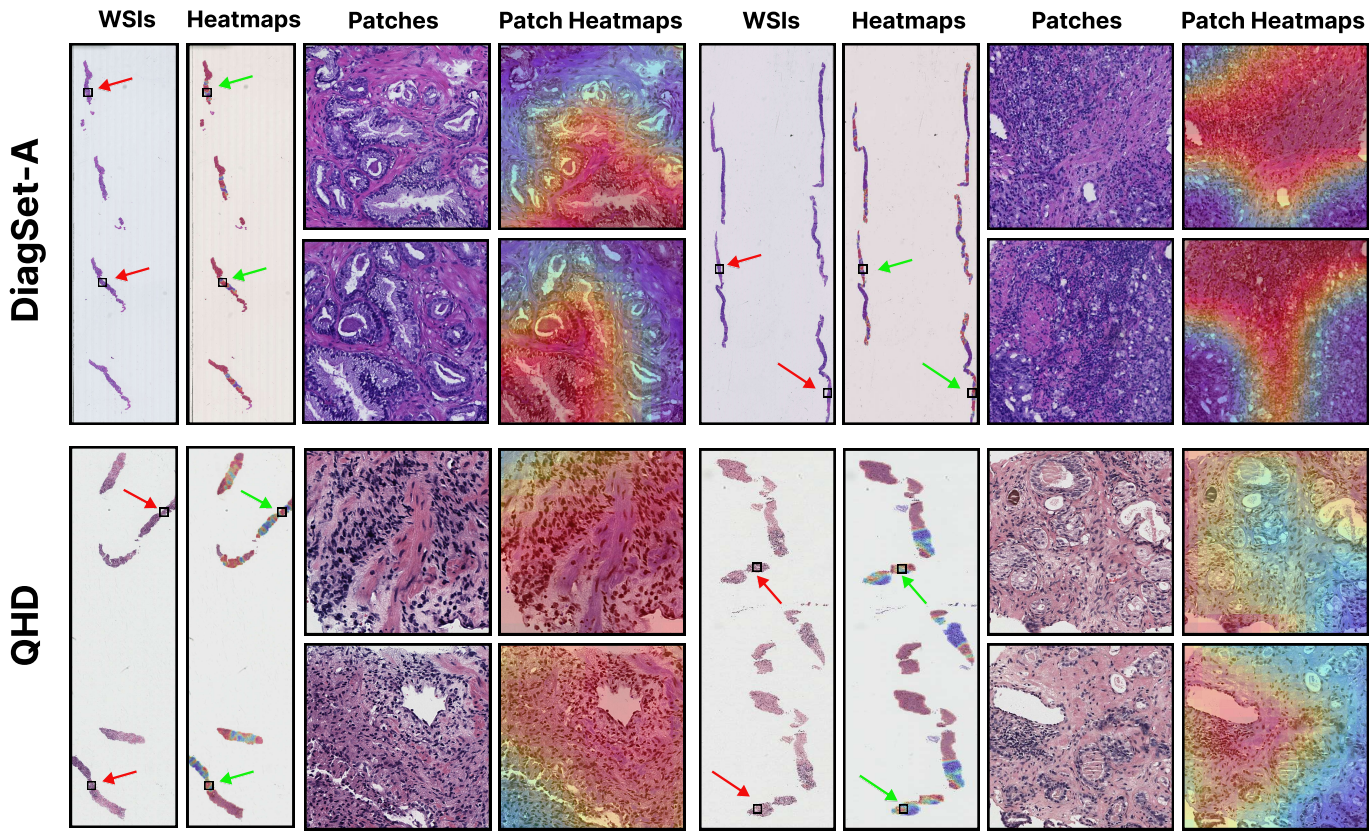


Fig. 4. Interpretability and visualization of FACL. Displayed are randomized selections of WSIs from external datasets, DiagSet-A and QHD, arranged in the first and second rows, respectively. The sequence progresses from left to right, showcasing the complete WSI, followed by its heatmap, a close-up of a local patch, and finally, the heatmap of the patch. The zoomed-in view of the local patch image underscores our model’s precise identification and representation of cancerous regions.

in collaboration with medical institutions spanning different regions, facilitating FL in pathology image tasks and enabling a globally intelligent approach to rare disease diagnosis. Furthermore, as our current work has been conducted in a simulated environment, we recognize the need to consider communication efficiency in a real-world system. In a FL environment, training data remains distributed among numerous centers, each with potentially unreliable and relatively slow network connections. Overcoming the challenges of privacy, security, and communication efficiency associated with FL is crucial to drive further advancements in the healthcare industry.

Acknowledgments

This research is supported in part by Science, Technology and Innovation Commission of Shenzhen Municipality (No. WDZC20200818121348001).

Ethics approval and consent to participate

The Research Ethics Committee of The Fourth Hospital of Hebei Medical University, China, approved this study.

Availability of data and materials

The private test data during the current study is not publicly available due to restrictions in the ethical permit. PANDA can be accessed at <https://www.kaggle.com/c/prostate-cancer-grade-assessment>. Diagset can be accessed at <https://ai-econsilio.diag.pl/>. The computer code of the deep learning model will be available for publishing.

References

- [1] H. Sung, J. Ferlay, R. L. Siegel, M. Laversanne, I. Soerjomataram, A. Jemal, and F. Bray, “Global cancer statistics 2020: Globocan estimates of incidence and mortality worldwide for 36 cancers in 185 countries,” *CA: a cancer journal for clinicians*, vol. 71, no. 3, pp. 209–249, 2021.
- [2] C. Lu and M. Mandal, “Automated analysis and diagnosis of skin melanoma on whole slide histopathological images,” *Pattern Recognition*, vol. 48, no. 8, pp. 2738–2750, 2015.
- [3] Y. Schirris, E. Gavves, I. Nederlof, H. M. Horlings, and J. Teuwen, “Deepsmile: Contrastive self-supervised pre-training benefits msi and hrd classification directly from h&e whole-slide images in colorectal and breast cancer,” *Medical Image Analysis*, vol. 79, p. 102464, 2022.
- [4] P. Chikontwe, S. J. Nam, H. Go, M. Kim, H. J. Sung, and S. H. Park, “Feature re-calibration based multiple instance learning for whole slide image classification,” in *International Conference on Medical Image Computing and Computer-Assisted Intervention*. Springer, 2022, pp. 420–430.
- [5] K. Kartasalo, W. Bulten, B. Delahunt, P.-H. C. Chen, H. Pinckaers, H. Olsson, X. Ji, N. Mulliqi, H. Samaratunga, T. Tsuzuki *et al.*, “Artificial intelligence for diagnosis and gleason grading of prostate cancer in

biopsies—current status and next steps,” *European Urology Focus*, vol. 7, no. 4, pp. 687–691, 2021.

[6] X. Ma, L. Chen, T. Chen, K. Chen, H. Zhang, K. Huang, H. Zheng, H. Jin, Z. Cheng, K. Xiao *et al.*, “Identification of a 24-gene panel and a novel marker of podxl2 essential for the pathological diagnosis of early prostate cancer,” *Computational and Structural Biotechnology Journal*, vol. 21, pp. 5476–5490, 2023.

[7] B. Delahunt, R. J. Miller, J. R. Srigley, A. J. Evans, and H. Samaratunga, “Gleason grading: past, present and future,” *Histopathology*, vol. 60, no. 1, pp. 75–86, 2012.

[8] J. Silva-Rodríguez, A. Colomer, M. A. Sales, R. Molina, and V. Naranjo, “Going deeper through the gleason scoring scale: An automatic end-to-end system for histology prostate grading and cribriform pattern detection,” *Computer Methods and Programs in Biomedicine*, vol. 195, p. 105637, 2020.

[9] E. Short, A. Y. Warren, and M. Varma, “Gleason grading of prostate cancer: a pragmatic approach,” *Diagnostic Histopathology*, vol. 25, no. 10, pp. 371–378, 2019.

[10] R. S. George, A. Htoo, M. Cheng, T. M. Masterson, K. Huang, N. Adra, H. Z. Kaimakliotis, M. Akgul, and L. Cheng, “Artificial intelligence in prostate cancer: Definitions, current research, and future directions,” *Urologic Oncology: Seminars and Original Investigations*, vol. 40, no. 6, pp. 262–270, 2022. [Online]. Available: <https://www.sciencedirect.com/science/article/pii/S1078143922000771>

[11] G. Campanella, M. G. Hanna, L. Geneslaw, A. Miraflor, V. Werneck Krauss Silva, K. J. Busam, E. Brogi, V. E. Reuter, D. S. Klimstra, and T. J. Fuchs, “Clinical-grade computational pathology using weakly supervised deep learning on whole slide images,” *Nature medicine*, vol. 25, no. 8, pp. 1301–1309, 2019.

[12] X. Wang, J. Xiang, J. Zhang, S. Yang, Z. Yang, M.-H. Wang, J. Zhang, Y. Wei, J. Huang, and X. Han, “SCL-WC: Cross-slide contrastive learning for weakly-supervised whole-slide image classification,” in *Advances in Neural Information Processing Systems*, A. H. Oh, A. Agarwal, D. Belgrave, and K. Cho, Eds., 2022. [Online]. Available: <https://openreview.net/forum?id=1fKJLRTUdo>

[13] X. Wang, Y. Du, S. Yang, J. Zhang, M. Wang, J. Zhang, W. Yang, J. Huang, and X. Han, “Retccl: Clustering-guided contrastive learning for whole-slide image retrieval,” *Medical Image Analysis*, vol. 83, p. 102645, 2023.

[14] J. Xiang, X. Wang, X. Wang, J. Zhang, S. Yang, W. Yang, X. Han, and Y. Liu, “Automatic diagnosis and grading of prostate cancer with weakly supervised learning on whole slide images,” *Computers in Biology and Medicine*, vol. 152, p. 106340, 2023.

[15] W. Bulten, K. Kartasalo, P.-H. C. Chen, P. Ström, H. Pinckaers, K. Nagpal, Y. Cai, D. F. Steiner, H. van Boven, R. Vink *et al.*, “Artificial intelligence for diagnosis and gleason grading of prostate cancer: the panda challenge,” *Nature medicine*, vol. 28, no. 1, pp. 154–163, 2022.

[16] W. Bulten, H. Pinckaers, H. van Boven, R. Vink, T. de Bel, B. van Ginneken, J. van der Laak, C. Hulsbergen-van de Kaa, and G. Litjens, “Automated deep-learning system for gleason grading of prostate cancer using biopsies: a diagnostic study,” *The Lancet Oncology*, vol. 21, no. 2, pp. 233–241, 2020.

[17] Y. Takahashi, E. Dungubat, H. Kusano, and T. Fukusato, “Artificial intelligence and deep learning: New tools for histopathological diagnosis of nonalcoholic fatty liver disease/nonalcoholic steatohepatitis,” *Computational and Structural Biotechnology Journal*, 2023.

[18] S. Perincheri, A. W. Levi, R. Celli, P. Gershkovich, D. Rimm, J. S. Morrow, B. Rothrock, P. Raciti, D. Klimstra, and J. Sinard, “An independent assessment of an artificial intelligence system for prostate cancer detection shows strong diagnostic accuracy,” *Modern Pathology*, vol. 34, no. 8, pp. 1588–1595, 2021.

[19] K. Nagpal, D. Foote, F. Tan, Y. Liu, P.-H. C. Chen, D. F. Steiner, N. Manoj, N. Olson, J. L. Smith, A. Mohtashamian *et al.*, “Development and validation of a deep learning algorithm for gleason grading of prostate cancer from biopsy specimens,” *JAMA oncology*, vol. 6, no. 9, pp. 1372–1380, 2020.

[20] L. Pantanowitz, G. M. Quiroga-Garza, L. Bien, R. Heled, D. Laifenfeld, C. Linhart, J. Sandbank, A. A. Shach, V. Shalev, M. Vecsler *et al.*, “An artificial intelligence algorithm for prostate cancer diagnosis in whole slide images of core needle biopsies: a blinded clinical validation and deployment study,” *The Lancet Digital Health*, vol. 2, no. 8, pp. e407–e416, 2020.

[21] Y. Mun, I. Paik, S.-J. Shin, T.-Y. Kwak, and H. Chang, “Yet another automated gleason grading system (yaaggs) by weakly supervised deep learning,” *npj Digital Medicine*, vol. 4, no. 1, pp. 1–9, 2021.

[22] H. S. Muti, L. R. Heij, G. Keller, M. Kohlruss, R. Langer, B. Dislich, J.-H. Cheong, Y.-W. Kim, H. Kim, M.-C. Kook *et al.*, “Development and validation of deep learning classifiers to detect epstein-barr virus and microsatellite instability status in gastric cancer: a retrospective multicentre cohort study,” *The Lancet Digital Health*, vol. 3, no. 10, pp. e654–e664, 2021.

[23] A. Echle, H. I. Grabsch, P. Quirke, P. A. van den Brandt, N. P. West, G. G. Hutchins, L. R. Heij, X. Tan, S. D. Richman, J. Krause *et al.*, “Clinical-grade detection of microsatellite instability in colorectal tumors by deep learning,” *Gastroenterology*, vol. 159, no. 4, pp. 1406–1416, 2020.

[24] O. L. Saldanha, P. Quirke, N. P. West, J. A. James, M. B. Loughrey, H. I. Grabsch, M. Salto-Tellez, E. Alwers, D. Cifci, N. Ghaffari Laleh *et al.*, “Swarm learning for decentralized artificial intelligence in cancer histopathology,” *Nature Medicine*, pp. 1–8, 2022.

[25] S. Pati, U. Baid, B. Edwards, M. Sheller, S.-H. Wang, G. A. Reina, P. Foley, A. Gruzdov, D. Karkada, C. Davatzikos *et al.*, “Federated learning enables big data for rare cancer boundary detection,” *Nature communications*, vol. 13, no. 1, pp. 1–17, 2022.

[26] Q. Liu, H. Yang, Q. Dou, and P.-A. Heng, “Federated semi-supervised medical image classification via inter-client relation matching,” in *International Conference on Medical Image Computing and Computer-Assisted Intervention*. Springer, 2021, pp. 325–335.

[27] T. Li, A. K. Sahu, A. Talwalkar, and V. Smith, “Federated learning: Challenges, methods, and future directions,” *IEEE Signal Processing Magazine*, vol. 37, no. 3, pp. 50–60, 2020.

[28] J. Xu, B. S. Glicksberg, C. Su, P. Walker, J. Bian, and F. Wang, “Federated learning for healthcare informatics,” *Journal of Healthcare Informatics Research*, vol. 5, no. 1, pp. 1–19, 2021.

[29] M. J. Sheller, B. Edwards, G. A. Reina, J. Martin, S. Pati, A. Kotrotsou, M. Milchenko, W. Xu, D. Marcus, R. R. Colen *et al.*, “Federated learning in medicine: facilitating multi-institutional collaborations without sharing patient data,” *Scientific reports*, vol. 10, no. 1, pp. 1–12, 2020.

[30] N. Rieke, J. Hancox, W. Li, F. Milletari, H. R. Roth, S. Albarqouni, S. Bakas, M. N. Galtier, B. A. Landman, K. Maier-Hein *et al.*, “The future of digital health with federated learning,” *NPJ digital medicine*, vol. 3, no. 1, pp. 1–7, 2020.

[31] M. Y. Lu, R. J. Chen, D. Kong, J. Lipkova, R. Singh, D. F. Williamson, T. Y. Chen, and F. Mahmood, “Federated learning for computational pathology on gigapixel whole slide images,” *Medical image analysis*, vol. 76, p. 102298, 2022.

[32] T. S. Brisimi, R. Chen, T. Mela, A. Olshevsky, I. C. Paschalidis, and W. Shi, “Federated learning of predictive models from federated electronic health records,” *International journal of medical informatics*, vol. 112, pp. 59–67, 2018.

[33] S. Boughorbel, F. Jarray, N. Venugopal, S. Moosa, H. Elhadi, and M. Makhlof, “Federated uncertainty-aware learning for distributed hospital ehr data,” *arXiv preprint arXiv:1910.12191*, 2019.

[34] L. Huang, A. L. Shea, H. Qian, A. Masurkar, H. Deng, and D. Liu, “Patient clustering improves efficiency of federated machine learning to predict mortality and hospital stay time using distributed electronic medical records,” *Journal of biomedical informatics*, vol. 99, p. 103291, 2019.

[35] X. Min, B. Yu, and F. Wang, “Predictive modeling of the hospital readmission risk from patients’ claims data using machine learning: a case study on copd,” *Scientific reports*, vol. 9, no. 1, pp. 1–10, 2019.

[36] R. Duan, M. R. Boland, Z. Liu, Y. Liu, H. H. Chang, H. Xu, H. Chu, C. H. Schmid, C. B. Forrest, J. H. Holmes *et al.*, “Learning from electronic health records across multiple sites: A communication-efficient and privacy-preserving distributed algorithm,” *Journal of the American Medical Informatics Association*, vol. 27, no. 3, pp. 376–385, 2020.

[37] Y. Chen, X. Qin, J. Wang, C. Yu, and W. Gao, “Fedhealth: A federated transfer learning framework for wearable healthcare,” *IEEE Intelligent Systems*, vol. 35, no. 4, pp. 83–93, 2020.

[38] E. Brophy, M. De Vos, G. Boylan, and T. Ward, “Estimation of continuous blood pressure from ppg via a federated learning approach,” *Sensors*, vol. 21, no. 18, p. 6311, 2021.

[39] O. Choudhury, Y. Park, T. Saloniidis, A. Gkoulalas-Divanis, I. Sylla *et al.*, “Predicting adverse drug reactions on distributed health data using federated learning,” in *AMIA Annual symposium proceedings*, vol. 2019. American Medical Informatics Association, 2019, p. 313.

[40] S. Chen, D. Xue, G. Chuai, Q. Yang, and Q. Liu, “Fl-qsar: a federated learning-based qsar prototype for collaborative drug discovery,” *Bioinformatics*, vol. 36, no. 22–23, pp. 5492–5498, 2021.

[41] Z. Xiong, Z. Cheng, X. Lin, C. Xu, X. Liu, D. Wang, X. Luo, Y. Zhang, H. Jiang, N. Qiao *et al.*, “Facing small and biased data dilemma in drug discovery with enhanced federated learning approaches,” *Science China Life Sciences*, vol. 65, no. 3, pp. 529–539, 2022.

[42] B. Yan, J. Wang, J. Cheng, Y. Zhou, Y. Zhang, Y. Yang, L. Liu, H. Zhao, C. Wang, and B. Liu, “Experiments of federated learning for covid-19 chest x-ray images,” in *International Conference on Artificial Intelligence and Security*. Springer, 2021, pp. 41–53.

[43] I. Feki, S. Ammar, Y. Kessentini, and K. Muhammad, “Federated learning for covid-19 screening from chest x-ray images,” *Applied Soft Computing*, vol. 106, p. 107330, 2021.

[44] H. Lee, Y. J. Chai, H. Joo, K. Lee, J. Y. Hwang, S.-M. Kim, K. Kim, I.-C. Nam, J. Y. Choi, H. W. Yu *et al.*, “Federated learning for thyroid ultrasound image analysis to protect personal information: Validation study in a real health care environment,” *JMIR medical informatics*, vol. 9, no. 5, p. e25869, 2021.

[45] Q. Dou, T. Y. So, M. Jiang, Q. Liu, V. Vardhanabhoti, G. Kaassis, Z. Li, W. Si, H. H. Lee, K. Yu *et al.*, “Federated deep learning for detecting covid-19 lung abnormalities in ct: a privacy-preserving multinational validation study,” *NPJ digital medicine*, vol. 4, no. 1, pp. 1–11, 2021.

[46] L. M. Florescu, C. T. Streba, M.-S. Ţerbănescu, M. Mămăleanu, D. N. Florescu, R. V. Teică, R. E. Nica, and I. A. Gheonea, “Federated learning approach with pre-trained deep learning models for covid-19 detection from unsegmented ct images,” *Life*, vol. 12, no. 7, p. 958, 2022.

[47] P. Guo, P. Wang, J. Zhou, S. Jiang, and V. M. Patel, “Multi-institutional collaborations for improving deep learning-based magnetic resonance image reconstruction using federated learning,” in *Proceedings of the IEEE/CVF Conference on Computer Vision and Pattern Recognition*, 2021, pp. 2423–2432.

[48] D. Stripelis, J. L. Ambite, P. Lam, and P. Thompson, “Scaling neuroscience research using federated learning,” in *2021 IEEE 18th International Symposium on Biomedical Imaging (ISBI)*. IEEE, 2021, pp. 1191–1195.

[49] I. Shiri, A. V. Sadr, A. Sanaat, S. Ferdowsi, H. Arabi, and H. Zaidi, “Federated learning-based deep learning model for pet attenuation and scatter correction: a multi-center study,” in *2021 IEEE Nuclear Science Symposium and Medical Imaging Conference (NSS/MIC)*. IEEE, 2021, pp. 1–3.

[50] M. Andreux, J. O. d. Terrail, C. Beguier, and E. W. Tramel, “Siloed federated learning for multi-centric histopathology datasets,” in *Domain Adaptation and Representation Transfer, and Distributed and Collaborative Learning*. Springer, 2020, pp. 129–139.

[51] M. Adnan, S. Kalra, J. C. Cresswell, G. W. Taylor, and H. R. Tizhoosh, “Federated learning and differential privacy for medical image analysis,” *Scientific reports*, vol. 12, no. 1, pp. 1–10, 2022.

[52] X. Wang, J. Zhang, S. Yang, J. Xiang, F. Luo, M. Wang, J. Zhang, W. Yang, J. Huang, and X. Han, “A generalizable and robust deep learning algorithm for mitosis detection in multicenter breast histopathological images,” *Medical Image Analysis*, vol. 84, p. 102703, 2023.

[53] U. Baid, S. Pati, T. M. Kure, R. Gupta, E. Bremer, S. Abousamra, S. P. Thakur, J. H. Saltz, and S. Bakas, “Federated learning for the classification of tumor infiltrating lymphocytes,” *arXiv preprint arXiv:2203.16622*, 2022.

[54] J. Ogier du Terrail, A. Leopold, C. Joly, C. Béguier, M. Andreux, C. Maussion, B. Schmauch, E. W. Tramel, E. Bendjebar, M. Zaslavskiy *et al.*, “Federated learning for predicting histological response to neoadjuvant chemotherapy in triple-negative breast cancer,” *Nature Medicine*, pp. 1–12, 2023.

[55] P. Kairouz, H. B. McMahan, B. Avent, A. Bellet, M. Bennis, A. N. Bhagoji, K. Bonawitz, Z. Charles, G. Cormode, R. Cummings *et al.*, “Advances and open problems in federated learning,” *Foundations and Trends® in Machine Learning*, vol. 14, no. 1–2, pp. 1–210, 2021.

[56] A. B. de Luca, G. Zhang, X. Chen, and Y. Yu, “Mitigating data heterogeneity in federated learning with data augmentation,” *arXiv preprint arXiv:2206.09979*, 2022.

[57] S. Ahn, S. Kim, Y. Kwon, J. Park, J. Youn, and S. Cho, “Communication-efficient diffusion strategy for performance improvement of federated learning with non-iid data,” *arXiv preprint arXiv:2207.07493*, 2022.

[58] H. Nguyen, L. Phan, H. Warrier, and Y. Gupta, “Federated learning for non-iid data via client variance reduction and adaptive server update,” *arXiv preprint arXiv:2207.08391*, 2022.

[59] B. McMahan, E. Moore, D. Ramage, S. Hampson, and B. A. y Arcas, “Communication-efficient learning of deep networks from decentralized data,” in *Artificial intelligence and statistics*. PMLR, 2017, pp. 1273–1282.

[60] X.-C. Li and D.-C. Zhan, “Fedrs: Federated learning with restricted softmax for label distribution non-iid data,” in *Proceedings of the 27th ACM SIGKDD Conference on Knowledge Discovery & Data Mining*, 2021, pp. 995–1005.

[61] L. Gao, H. Fu, L. Li, Y. Chen, M. Xu, and C.-Z. Xu, “Feddc: Federated learning with non-iid data via local drift decoupling and correction,” in *Proceedings of the IEEE/CVF Conference on Computer Vision and Pattern Recognition*, 2022, pp. 10112–10121.

[62] F. Hanzely, B. Zhao, and M. Kolar, “Personalized federated learning: A unified framework and universal optimization techniques,” *arXiv preprint arXiv:2102.09743*, 2021.

[63] X. Wu, Y. Zhang, M. Shi, P. Li, R. Li, and N. N. Xiong, “An adaptive federated learning scheme with differential privacy preserving,” *Future Generation Computer Systems*, vol. 127, pp. 362–372, 2022.

[64] C. Wang, X. Wu, G. Liu, T. Deng, K. Peng, and S. Wan, “Safeguarding cross-silo federated learning with local differential privacy,” *Digital Communications and Networks*, vol. 8, no. 4, pp. 446–454, 2022.

[65] C. Dwork, K. Kenthapadi, F. McSherry, I. Mironov, and M. Naor, “Our data, ourselves: Privacy via distributed noise generation,” in *Annual international conference on the theory and applications of cryptographic techniques*. Springer, 2006, pp. 486–503.

[66] J. Zhao, H. Zhu, F. Wang, R. Lu, H. Li, J. Tu, and J. Shen, “Cork: A privacy-preserving and lossless federated learning scheme for deep neural network,” *Information Sciences*, vol. 603, pp. 190–209, 2022.

[67] Q. Li, B. He, and D. Song, “Model-contrastive federated learning,” in *Proceedings of the IEEE/CVF Conference on Computer Vision and Pattern Recognition*, 2021, pp. 10713–10722.

[68] T. Li, A. K. Sahu, M. Zaheer, M. Sanjabi, A. Talwalkar, and V. Smith, “Federated optimization in heterogeneous networks,” *Proceedings of Machine Learning and Systems*, vol. 2, pp. 429–450, 2020.

[69] S. Malaviya, M. Shukla, P. Korat, and S. Lodha, “Fedfame: A data augmentation free framework based on model contrastive learning for federated semi-supervised learning,” in *Proceedings of the 38th ACM/SIGAPP Symposium on Applied Computing*, 2023, pp. 1114–1121.

[70] Z. Liu, F. Wu, Y. Wang, M. Yang, and X. Pan, “Fedcl: Federated contrastive learning for multi-center medical image classification,” *Pattern Recognition*, p. 109739, 2023.

[71] S. M. Hosseini, M. Sikaroudi, M. Babaie, and H. Tizhoosh, “Proportionally fair hospital collaborations in federated learning of histopathology images,” *IEEE Transactions on Medical Imaging*, 2023.

[72] S. M. Hosseini, M. Sikaroudi, M. Babaie, and H. R. Tizhoosh, “Cluster based secure multi-party computation in federated learning for histopathology images,” in *International Workshop on Distributed, Collaborative, and Federated Learning, Workshop on Affordable Healthcare and AI for Resource Diverse Global Health*. Springer, 2022, pp. 110–118.

[73] T. Chen, S. Kornblith, M. Norouzi, and G. Hinton, “A simple framework for contrastive learning of visual representations,” in *International conference on machine learning*. PMLR, 2020, pp. 1597–1607.

[74] K. He, H. Fan, Y. Wu, S. Xie, and R. Girshick, “Momentum contrast for unsupervised visual representation learning,” in *Proceedings of the IEEE/CVF conference on computer vision and pattern recognition*, 2020, pp. 9729–9738.

[75] R. Krishnan, P. Rajpurkar, and E. J. Topol, “Self-supervised learning in medicine and healthcare,” *Nature Biomedical Engineering*, pp. 1–7, 2022.

[76] T. Wanyan, H. Honavar, S. K. Jaladanki, C. Zang, N. Naik, S. Soman, J. K. De Freitas, I. Paranjpe, A. Vaid, J. Zhang *et al.*, “Contrastive learning improves critical event prediction in covid-19 patients,” *Patterns*, vol. 2, no. 12, p. 100389, 2021.

[77] R. Li and J. Gao, “Multi-modal contrastive learning for healthcare data analytics,” in *2022 IEEE 10th International Conference on Healthcare Informatics (ICHI)*. IEEE, 2022, pp. 120–127.

[78] C. I. Tang, I. Perez-Pozuelo, D. Spathis, and C. Mascolo, “Exploring contrastive learning in human activity recognition for healthcare,” *arXiv preprint arXiv:2011.11542*, 2020.

[79] N. Diamant, E. Reinertsen, S. Song, A. D. Aguirre, C. M. Stultz, and

P. Batra, "Patient contrastive learning: A performant, expressive, and practical approach to electrocardiogram modeling," *PLoS Computational Biology*, vol. 18, no. 2, p. e1009862, 2022.

[80] Y. N. T. Vu, R. Wang, N. Balachandar, C. Liu, A. Y. Ng, and P. Rajpurkar, "Medaug: Contrastive learning leveraging patient metadata improves representations for chest x-ray interpretation," in *Machine Learning for Healthcare Conference*. PMLR, 2021, pp. 755–769.

[81] K. Chaitanya, E. Erdil, N. Karani, and E. Konukoglu, "Contrastive learning of global and local features for medical image segmentation with limited annotations," *Advances in Neural Information Processing Systems*, vol. 33, pp. 12 546–12 558, 2020.

[82] S. Azizi, B. Mustafa, F. Ryan, Z. Beaver, J. Freyberg, J. Deaton, A. Loh, A. Karthikesalingam, S. Kornblith, T. Chen *et al.*, "Big self-supervised models advance medical image classification," in *Proceedings of the IEEE/CVF International Conference on Computer Vision*, 2021, pp. 3478–3488.

[83] B. Li, Y. Li, and K. W. Eliceiri, "Dual-stream multiple instance learning network for whole slide image classification with self-supervised contrastive learning," in *Proceedings of the IEEE/CVF conference on computer vision and pattern recognition*, 2021, pp. 14 318–14 328.

[84] J. Yan, H. Chen, X. Li, and J. Yao, "Deep contrastive learning based tissue clustering for annotation-free histopathology image analysis," *Computerized Medical Imaging and Graphics*, vol. 97, p. 102053, 2022.

[85] Z. Zhu, L. Yu, W. Wu, R. Yu, D. Zhang, and L. Wang, "Murcl: Multi-instance reinforcement contrastive learning for whole slide image classification," *IEEE Transactions on Medical Imaging*, 2022.

[86] P. A. Fashi, S. Hemati, M. Babaie, R. Gonzalez, and H. Tizhoosh, "A self-supervised contrastive learning approach for whole slide image representation in digital pathology," *Journal of Pathology Informatics*, vol. 13, p. 100133, 2022.

[87] X. Wang, S. Yang, J. Zhang, M. Wang, J. Zhang, W. Yang, J. Huang, and X. Han, "Transformer-based unsupervised contrastive learning for histopathological image classification," *Medical Image Analysis*, vol. 81, p. 102559, 2022.

[88] M. Ilse, J. Tomczak, and M. Welling, "Attention-based deep multiple instance learning," in *International conference on machine learning*. PMLR, 2018, pp. 2127–2136.

[89] X. Wang, D. Cai, S. Yang, Y. Cui, J. Zhu, K. Wang, and J. Zhao, "Sacnet: Enhancing spatiotemporal aggregation in cervical histological image classification via label-efficient weakly supervised learning," *IEEE Transactions on Circuits and Systems for Video Technology*, 2023.

[90] N. Otsu, "A threshold selection method from gray-level histograms," *IEEE Transactions on Systems, Man, and Cybernetics*, vol. 9, no. 1, pp. 62–66, 1979.

[91] J. M. Joyce, "Kullback-leibler divergence," in *International encyclopedia of statistical science*. Springer, 2011, pp. 720–722.

[92] A. Ziller, D. Usynin, R. Braren, M. Makowski, D. Rueckert, and G. Kaassis, "Medical imaging deep learning with differential privacy," *Scientific Reports*, vol. 11, no. 1, p. 13524, 2021.

[93] Q. Yang, Y. Liu, T. Chen, and Y. Tong, "Federated machine learning: Concept and applications," *ACM Transactions on Intelligent Systems and Technology (TIST)*, vol. 10, no. 2, pp. 1–19, 2019.

Appendix

Table S1. The diagnostic model's performance on DiagSet-A was reported as the five-fold mean.

α	Training settings	AUC	F1	ACC	Recall
/	Hebei-1	0.9664	0.8888	0.8899	0.8281
	Hebei-2	0.9539	0.8742	0.8524	0.9647
	Nanchang	0.9544	0.7483	0.6440	0.9955
0.05	DiagSet-B-1	0.9579	0.8134	0.8313	0.6916
	DiagSet-B-2	0.9628	0.8888	0.8899	0.8281
	PANDA-1	0.9474	0.8741	0.8711	0.8414
	PANDA-2	0.9596	0.6964	0.5386	0.9955
	FedAvg	0.9635	0.9079	0.8969	0.9559
	Centralized	0.9670	0.9082	0.9063	0.8722
0.1	DiagSet-B-1	0.9605	0.8940	0.8922	0.8546
	DiagSet-B-2	0.9637	0.8737	0.8782	0.7929
	PANDA-1	0.9498	0.9126	0.9063	0.9207
	PANDA-2	0.9572	0.8712	0.8477	0.9691
	FedAvg	0.9648	0.9204	0.9133	0.9427
	Centralized	0.9631	0.8619	0.8665	0.7841
0.3	DiagSet-B-1	0.9663	0.9062	0.9016	0.8942
	DiagSet-B-2	0.9684	0.8803	0.8829	0.8105
	PANDA-1	0.9541	0.8457	0.8103	0.9779
	PANDA-2	0.9614	0.8912	0.8782	0.9383
	FedAvg	0.9651	0.8972	0.8852	0.9427
	Centralized	0.9712	0.9162	0.9110	0.9162
0.5	DiagSet-B-1	0.9655	0.9027	0.9016	0.8590
	DiagSet-B-2	0.9686	0.9045	0.9016	0.8766
	PANDA-1	0.9488	0.7174	0.5831	0.9955
	PANDA-2	0.9617	0.9193	0.9133	0.9295
	FedAvg	0.9647	0.8957	0.8805	0.9647
	Centralized	0.9697	0.9115	0.9086	0.8854

Table S2. The diagnostic model's performance on QHD was reported as the five-fold mean.

α	Training settings	AUC	F1	ACC	Recall
/	Hebei-1	0.9636	0.9204	0.9150	0.8683
	Hebei-2	0.9805	0.8914	0.8653	0.9769
	Nanchang	0.9731	0.8201	0.7568	0.9792
0.05	DiagSet-B-1	0.9727	0.8274	0.8326	0.7090
	DiagSet-B-2	0.9734	0.8769	0.8745	0.7898
	PANDA-1	0.9769	0.8259	0.8313	0.7066
	PANDA-2	0.9838	0.7234	0.5673	1.0000
	FedAvg	0.9795	0.9439	0.9346	0.9722
	Centralized	0.9788	0.9467	0.9385	0.9653
0.1	DiagSet-B-1	0.9718	0.9268	0.9215	0.8775
	DiagSet-B-2	0.9736	0.8866	0.8836	0.8036
	PANDA-1	0.9766	0.9407	0.9333	0.9353
	PANDA-2	0.9778	0.7487	0.6209	0.9976
	FedAvg	0.9775	0.9426	0.9333	0.9676
	Centralized	0.9731	0.9477	0.9398	0.9630
0.3	DiagSet-B-1	0.9761	0.9247	0.9202	0.8661
	DiagSet-B-2	0.9773	0.8953	0.8915	0.8198
	PANDA-1	0.9727	0.8782	0.8471	0.9745
	PANDA-2	0.9785	0.9442	0.9359	0.9584
	FedAvg	0.9788	0.9523	0.9451	0.9699
	Centralized	0.9802	0.9501	0.9424	0.9676
0.5	DiagSet-B-1	0.9761	0.9129	0.9084	0.8475
	DiagSet-B-2	0.9765	0.9323	0.9267	0.8914
	PANDA-1	0.9722	0.7386	0.6013	0.9953
	PANDA-2	0.9776	0.9512	0.9450	0.9468
	FedAvg	0.9765	0.9522	0.9451	0.9676
	Centralized	0.9766	0.9532	0.9464	0.9653